MRS Advances
https://doi.org/10.1557/s43580-022-00358-4

ORIGINAL PAPER

Role of heterostacking of 2D lead chloride perovskites on photoluminescence

David R. Graupner[1] · Dmitri S. Kilin[1]

Received: 8 June 2022 / Accepted: 17 October 2022

Abstract

Two-dimensional organic–inorganic hybrid lead halide perovskites are of interest for photovoltaic and light-emitting devices due to their favorable properties that can be tuned. Here, we use density functional theory to model two-dimensional lead halide perovskites of different thicknesses and combined into vertical heterostructures. Excited-state dynamics treated by reduced density matrix method is used to examine the excited-state optoelectronic properties of the perovskite models. Nonadiabatic couplings were computed based on the on-the-fly approach along a molecular dynamics trajectory at ambient temperatures. The dynamics of electronic degrees of freedom were calculated using density matrix-based equation of motion for electronic degrees of freedom. We observe that the vertical stacking of two-dimensional perovskites into heterostructures shows an increase in photoluminescence intensity by two orders of magnitude when compared to the individual two-dimensional perovskites.

Introduction

Two-dimensional (2D) $CsPbX_3$ (X = Cl, Br, I) organic–inorganic hybrid lead halide perovskites (LHPs) have become popular candidates for next-generation optoelectronic devices due to their favorable optoelectronic properties [1, 2] and increased stability when compared to the bulk LHPs [3]. Room-temperature perovskite light-emitting diodes (LEDs) were first reported in 2014 [4] and have shown impressive progress with 2D perovskite LEDs achieving 20.2% external quantum efficiency (EQE) in 2020 [5]. While there has been an increase in EQE for perovskite LEDs, there is still a need to generate high efficiency perovskite LEDs for pure colors to meet commercial viability [6, 7].

2D perovskites structures possess natural quantum-well structures that induce both dielectric and quantum confinement effects [8]. The strong confinements lead to large exciton binding energies [9]. Further, it is observed that 2D perovskites often form in a mixed-phase structures rather than a single phase structures due to the similar formation energies of the different thickness 2D perovskites [10]. The mixed-phase 2D perovskites result in heterostructures that offer the possibilities of manipulation of the recombination, transport, and generation of charge carriers due to the change in band gap energies at the heterojunction [11].

2D halide perovskites are defined by a stoichiometric formula, $A'_{n'}A_{n-1}M_nX_{3n+1}$ (A' = monovalent or divalent cation; $n' = 2$ or 1; $A = Cs^+$, methylammonium (MA), formadamidinium (FA); $M = Pb^{2+}$, Sn^{2+}, etc.; $X = Cl^-$, Br^-, I^-), and are classified based on the thickness of the inorganic layer as indicated in the stochiometric formula ($n = 1, 2, 3$, etc.) [12]. Different categories for the layered structures of 2D perovskites are defined based on the relative stacking of the layers; Dion–Jacobson (DJ) phase [13, 14], Ruddlesden–Popper (RP) phase [15], and Aurivilius phase [16]. The DJ perovskites show the ability to stack with no displacement due to the divalent interlayer spacers. The models examined in this paper are DJ perovskites with $n = 1$ or 4, Cs^+ for A, butyl diammonium (BdA) molecules as A', and Cl^- for X. The heterostructure model is a vertical stacking of the separate $n = 1$ and $n = 4$ models into a single model preserving the alternating organic and perovskite layers (Fig. 1). We start with chlorine providing smaller unit cell, with bromine and iodine models to follow.

Here, we report the effects that combining 2D DJ LHPs into a vertical heterostructure provide for the photoluminescence (PL) of the materials. The combination of the different size layers is expected to create an insulating effect that will increase the photoluminescence quantum yield (PLQY) of

✉ Dmitri S. Kilin
dmitri.kilin@ndsu.edu

[1] Department of Chemistry and Biochemistry, North Dakota State University, Fargo, ND 58108, USA

Published online: 07 November 2022

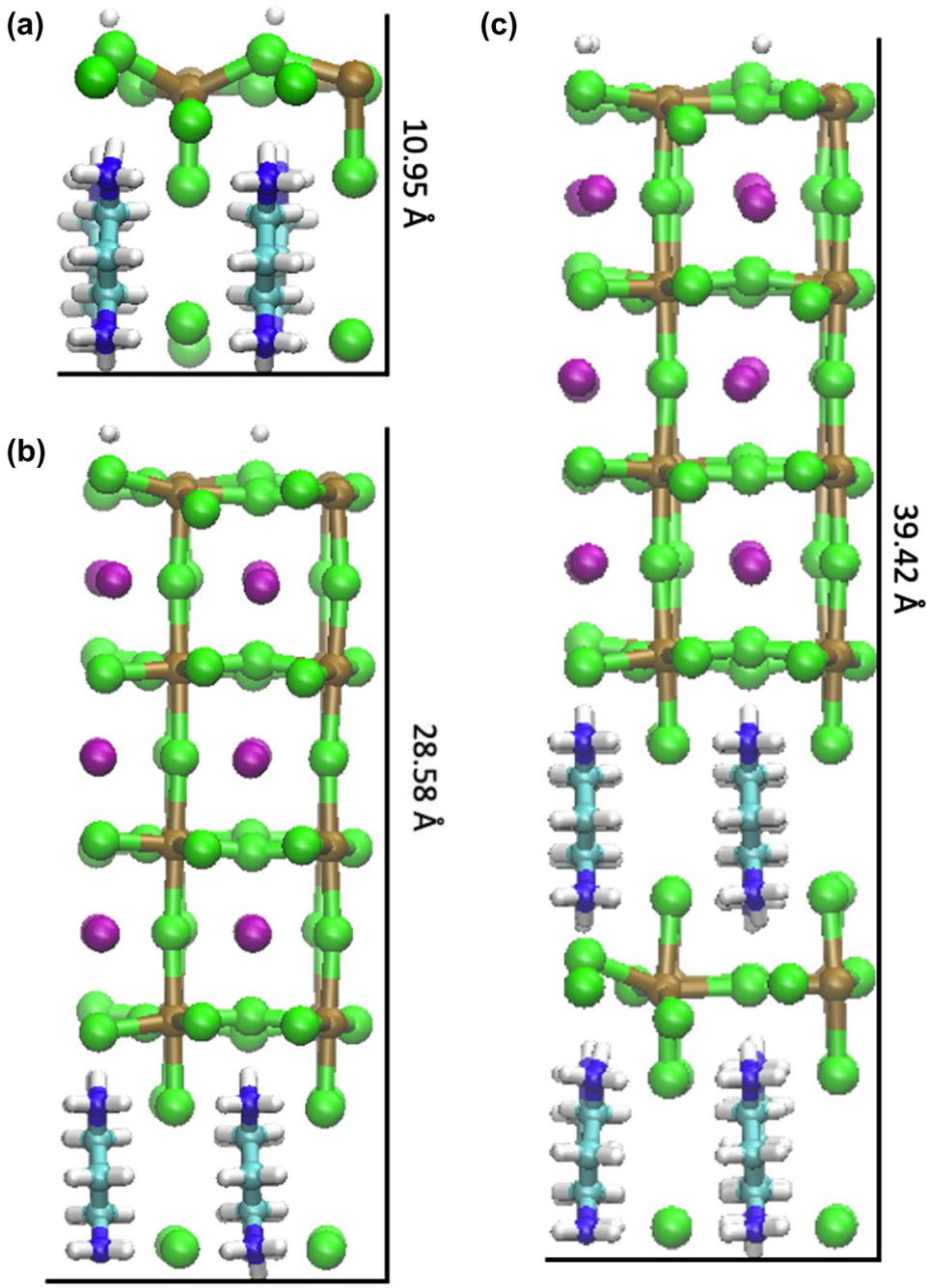

Fig. 1 Atomistic models of lead chloride organic–inorganic hybrid perovskite. Two models contain a single layer of perovskite where thickness of the perovskite layer is **a** $n=1$ and **b** $n=4$. The third model is a **c** vertical heterostructure that contains both a $n=1$ and $n=4$ perovskite layer. White, cyan, blue, brown, green, and purple spheres represent hydrogen, carbon, nitrogen, lead, chlorine, and cesium atoms, respectively

the thicker layer involved in the heterostructure. Nonadiabatic couplings (NACs) between nuclear and electronic degrees of freedom from adiabatic molecular dynamics trajectories are computed to calculate the excited-state dynamics and are used to characterize the effect of the heterostructure on PL properties. The reduced density matrix formalism within Redfield theory is used to compute nonradiative relaxation rates from the NACs [17]. PLQY is then computed from the nonradiative and radiative recombination rates, computed from Einstein coefficients.

Methods

Computational details

The ground-state electronic structure was calculated using DFT with the generalized gradient approximation (GGA) Perdew–Burke–Ernzerhof (PBE) functional [18] in a plane-wave basis set along with projector augmented-wave (PAW) pseudopotentials [19, 20] in Vienna Ab initio Simulation Package (VASP) [21]. Subsequent single-point

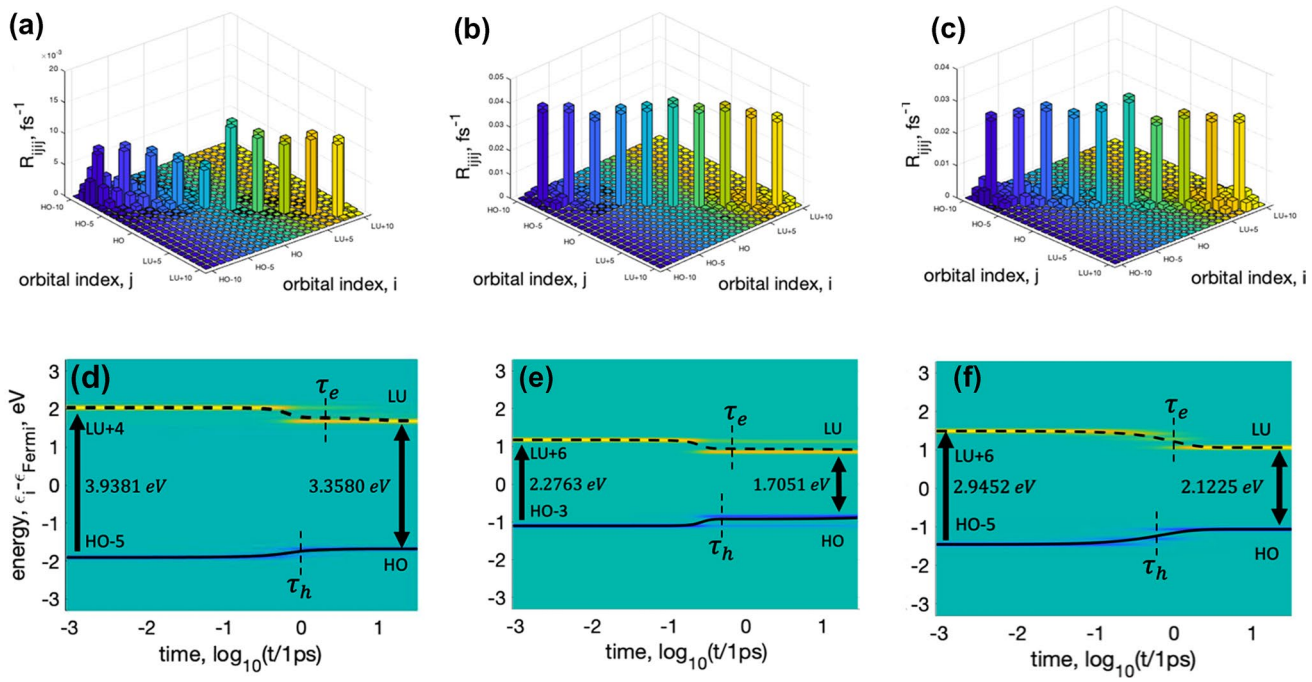

Fig. 2 Redfield tensor for **a** $n=1$ single layer, **b** $n=4$ single layer, and **c** heterostructure models. The R_{ijij} axis represents the nonradiative state-to-state transition rates. Nonradiative relaxation for the **d** $n=1$ single layer, **e** $n=4$ single layer, and **f** heterostructure models. The green color indicates background reference charge density. The yellow line represents the charge density of the electron, while the blue line represents the charge density of the hole. The vertical dashed lines labeled with τ_h and τ_e represent time of relaxation from HO $-x$ and LU $+y$, respectively. The horizontal solid and dashed lines show the energy expectation value for the hole and electron, respectively. The initial conditions for the $n=1$ and $n=4$ single layer models represent the highest oscillator strength excitation that does not involve one of the near-degenerate principal bandgap orbitals. The initial condition for the heterostructure model represents the highest oscillator strength transition that occurs on the $n=1$ layer in the model

calculations were performed using noncollinear spin DFT including the spin–orbit coupling (SOC) interaction and used to compute observables for the systems. The model has a structure of $BdA_4Cs_{4(n-1)}Pb_{4n}Cl_{12n+4}$ with a simulation cell size of $10\times10\times(6+5.5n)$ Å. All calculations were performed at the Γ point. A single-point calculation takes approximately an hour of a walltime at 8 nodes with 64 cpu cores each.

Theory

Details of the electronic basis and computed observables are provided in the supplemental information (SI).

Results and discussion

Figure S1 panels (a, b) show the ground-state density of states (DOS) for the three models studied here, (c) shows projected DOS for the heterostructure model, and (d) shows the computed absorption spectra. The heterostructure model shows a similar pattern of peaks when compared to the $n=4$ single layer model for both the DOS and absorption spectra but higher in energy. The trends in absorption qualitatively align with those reported by Fu et al. [22] The projected DOS for the heterostructure model shows that the first band for both the conduction and valence band is localized on the $n=4$ layer of the heterostructure.

The Redfield tensors, R_{ijij}, depend on the NACs and are illustrated in Fig. 2 for the (a) $n=1$ single layer, (b) $n=4$ single layer, and (c) heterostructure models. The Redfield tensors represent the rates of state-to-state transitions in units of ps^{-1}. A pattern of alternating high intensity transitions are between near-degenerate states, which result from the inclusion of spin–orbit coupling into the calculations. Figure 2d–f shows hot-carrier cooling along the excited-state trajectory (d) for $n=1$ single layer, (e) $n=4$ single layer, and (f) heterostructure models from a nonequilibrium state to the first excited state. The SKSOs for the initial conditions and frontier orbitals are shown in Fig. S2. For the single layer models, it is observed that there is a long lived, compared to the $k_{e/h}$, population in a higher excited state than the first excited state. This is attributed to a mismatch between electronic transition energy and frequency of any available normal modes.

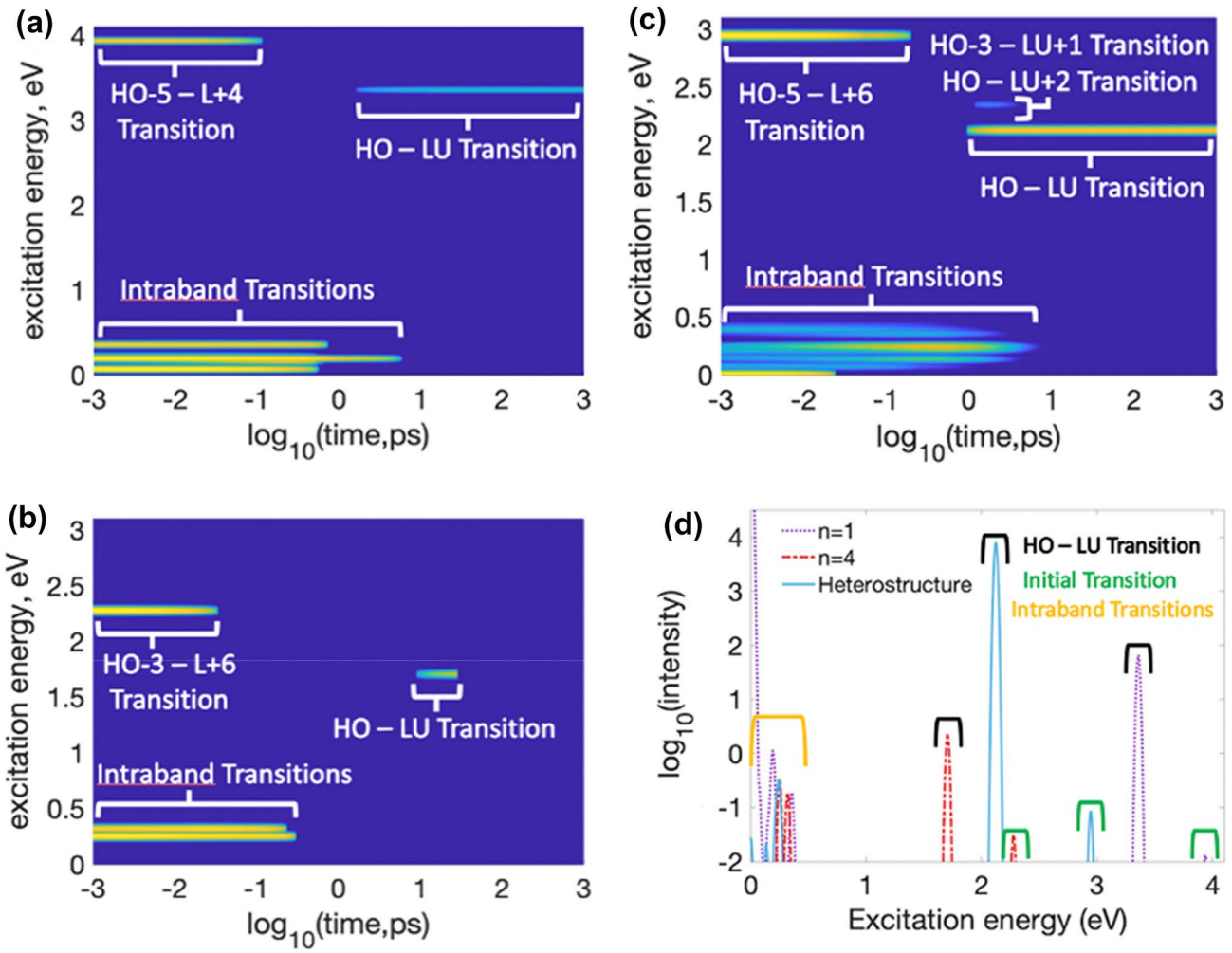

Fig. 3 Radiative relaxation along the excited-state electronic dynamics trajectory with **a–c** showing time-resolved emission for **a** $n=1$ single layer, **b** $n=4$ single layer, and **c** heterostructure models. **d** Time-integrated radiative emission for the models. The initial conditions are the same as those for Fig. 2. The blue background corresponds to no PL at a given time and transition energy. Natural colors from blue to yellow correspond to intensity of the time-resolved PL

A mechanism competing with nonradiative dissipation is radiative recombination in the form of emitting photons. Figure 3a–c shows the time-resolved emission, eq. S21, for the (a) $n=1$ single layer, (b) $n=4$ single layer, and (c) heterostructure models. Time-integrated emission, Eq. S22, for the models along the excited-state trajectory is shown in Fig. 3d. It is observed that there is an initial emission event at the initial excitation energy occurring before cooling to the bandgap. Once the hot-carriers cool to the bandgap we see emission arising from the transitions between the highest occupied (HO) and lowest unoccupied (LU) bands. It is observed that the emission at the HO–LU transition is the most intense for all the models. However, we observe that the intensity of the HO–LU transition for the heterostructure model is 2 orders of magnitude greater than the HO–LU transition for the $n=1$ single layer model and 3 orders of magnitude greater than for the $n=4$ single layer model. This increased intensity is attributed to the increased relative size of the spacer region of the structure as both the butyl diammonium layers and the $n=1$ layer have a larger bandgap than the $n=4$ layer. This isolation prevents hybridization of the electron and hole beyond the border of the slab and hypothetically confines the electron and hole in the same spatial region. This activity of the spacers is expected to increase the transition dipole, and by extension the oscillator strength.

The second highest intensity of emission for the heterostructure model occurs due to the HO-5–LU + 6 transition with an energy comparable to the HO–LU transition energy for the $n=1$ single layer model. This indicates that the heterostructure model may not follow Kasha's rule [23] and exhibits dual emission with energies that correspond to both

Table 1 Oscillator strength f_{ij}, radiative recombination rate k_r, nonradiative recombination rate k_{nr}, resultant PLQYs for each model studied

Model	f_{ij}	k_r [1/fs]	k_{nr} [1/fs]	PLQY
$n=1$ single layer	0.32	2.00×10^{-6}	1.86×10^{-6}	0.3326
$n=4$ single layer	0.07	2.64×10^{-6}	2.81×10^{-6}	0.3355
Heterostructure	0.60	3.22×10^{-6}	1.21×10^{-6}	0.6667

the $n=1$ and $n=4$ single layer models. This dual emission is in an agreement to the multiple emission found experimentally [22].

To determine the efficiency of PL for the single layer and heterostructure models, we compute PLQY, Eq. S24, from k_r and k_{nr}. The Einstein coefficient for spontaneous emission in terms of oscillator strength is used to calculate k_r, eq. S23, and the corresponding Redfield tensor element $R_{\text{HO–LU}}$ is used for k_{nr}, Eq. S16. Table 1 shows the k_r, k_{nr}, and PLQY for the models presented here. The oscillator strength shown here is for the HO–LU transition but the radiative and nonradiative rates of relaxation and PLQY shown factor in all four transitions between the near-degenerate HO–LU states. Due to this, we see a larger radiative recombination rate and PLQY for the $n=4$ single layer model than would be expected looking just at the oscillator strength reported in Table 1. The larger PLQY for the heterostructure is due to the smaller nonradiative recombination rate when compared to the single layer models and the consistent nature of the radiative recombination rate across these four transitions. The values for the each unique near-degenerate transition are seen in Table S1.

Conclusion

Here, we use density functional theory and nonadiabatic excited-state dynamics calculations to explore the photophysical properties of single layer and vertical heterostructures of two-dimensional hybrid lead chloride perovskites. The lesser degree of quantum confinement effect causes the $n=4$ region in the heterostructure model to be the major component of the results over the range of interest for energy that we investigated. We observed an increase in intensity of the photoluminescence for the vertical heterostructure 2D lead halide perovskites rationalized by the increase in effective insulation between the perovskite layers. The computed time-integrated photoluminescence spectra show that for the single layer models, there is a smaller relative intensity of emission across the band gap when compared to the vertical heterostructure model. The smaller intensity of photoluminescence in the single layer models is attributed to the smaller relative size of the space between layers allowing for a greater overlap of orbitals/bands/ between layers. In the heterostructure model, this space between the larger $n=4$ perovskite layers in adjacent periodic cells is made up of two organic layers and a smaller $n=1$ layer of perovskite, all of which have a larger gap than the $n=4$ perovskite layers. This increased separation prevents the overlap across multiple layers and confines the electron and hole in the same spatial region.

Supplementary Information The online version contains supplementary material available at https://doi.org/10.1557/s43580-022-00358-4.

Acknowledgments D.G. Thanks NSF CHE- 2004197 for support. D.K. acknowledges the support of the National Science Foundation under Grant CHE-1944921. The Authors thank the DOE BES NERSC facility for computational resources, allocation award "*Computational Modeling of Photo-catalysis and Photo-induced Charge Transfer Dynamics on Surfaces,*" supported by the Office of Science of the DOE under Contract DE-AC02-05CH11231. The Authors also thank Aaron Forde, Yulun Han, Landon Johnson, and Steven Westra for collective discussion and editing. D.K. thanks David Micha, Oleg Prezhdo, Sergei Tretiak, Svetlana Kilina, and Andrei Kryjevski for inspiring discussions.

Data availability Data will be made available on reasonable request.

Declarations

Conflict of interest The authors report there is no competing interests to declare.

References

1. L. Protesescu, S. Yakunin, M.I. Bodnarchuk, F. Krieg, R. Caputo, C.H. Hendon, R.X. Yang, A. Walsh, M.V. Kovalenko, Nano Lett. **15**, 3692–3696 (2015). https://doi.org/10.1021/nl5048779
2. T.M. Koh, V. Shanmugam, J. Schlipf, L. Oesinghaus, P. Muller-Buschbaum, N. Ramakrishnan, V. Swamy, N. Mathews, P.P. Boix, S.G. Mhaisalkar, Adv. Mater. **28**, 3653–3661 (2016). https://doi.org/10.1002/adma.201506141
3. F. Arabpour Roghabadi, M. Alidaei, S.M. Mousavi, T. Ashjari, A.S. Tehrani, V. Ahmadi, S.M. Sadrameli, J. Mater. Chem. A **7**, 5898–5933 (2019). https://doi.org/10.1039/C8TA10444A
4. Z.-K. Tan, R.S. Moghaddam, M.L. Lai, P. Docampo, R. Higler, F. Deschler, M. Price, A. Sadhanala, L.M. Pazos, D. Credgington, F. Hanusch, T. Bein, H.J. Snaith, R.H. Friend, Nat. Nanotechnol. **9**, 687–692 (2014). https://doi.org/10.1038/nnano.2014.149
5. Y. Miao, L. Cheng, W. Zou, L. Gu, J. Zhang, Q. Guo, Q. Peng, M. Xu, Y. He, S. Zhang, Y. Cao, R. Li, N. Wang, W. Huang, J. Wang, Light Sci. Appl. **9**, 89 (2020). https://doi.org/10.1038/s41377-020-0328-6
6. L. Zhang, C. Sun, T. He, Y. Jiang, J. Wei, Y. Huang, M. Yuan, Light: Sci. Appl. **10**, 61 (2021). https://doi.org/10.1038/s41377-021-00501-0
7. C. Zhao, D. Zhang, C. Qin, CCS Chem. **2**, 859–869 (2020). https://doi.org/10.31635/ccschem.020.202000216
8. K. Wang, J.Y. Park, Akriti, L. Dou, EcoMat **3**, e12104 (2021). https://doi.org/10.1002/eom2.12104

9. J.C. Blancon, A.V. Stier, H. Tsai, W. Nie, C.C. Stoumpos, B. Traoré, L. Pedesseau, M. Kepenekian, F. Katsutani, G.T. Noe, J. Kono, S. Tretiak, S.A. Crooker, C. Katan, M.G. Kanatzidis, J.J. Crochet, J. Even, A.D. Mohite, Nat. Commun. **9**, 2254 (2018). https://doi.org/10.1038/s41467-018-04659-x
10. L.N. Quan, M. Yuan, R. Comin, O. Voznyy, E.M. Beauregard, S. Hoogland, A. Buin, A.R. Kirmani, K. Zhao, A. Amassian, D.H. Kim, E.H. Sargent, J. Am. Chem. Soc. **138**, 2649–2655 (2016). https://doi.org/10.1021/jacs.5b11740
11. C.P. Clark, J.E. Mann, J.S. Bangsund, W.-J. Hsu, E.S. Aydil, R.J. Holmes, ACS Energy Lett. **5**, 3443–3451 (2020). https://doi.org/10.1021/acsenergylett.0c01609
12. L. Mao, W. Ke, L. Pedesseau, Y. Wu, C. Katan, J. Even, M.R. Wasielewski, C.C. Stoumpos, M.G. Kanatzidis, J. Am. Chem. Soc. **140**, 3775–3783 (2018). https://doi.org/10.1021/jacs.8b00542
13. M. Dion, M. Ganne, M. Tournoux, Mater. Res. Bull. **16**, 1429–1435 (1981). https://doi.org/10.1016/0025-5408(81)90063-5
14. A.J. Jacobson, J.W. Johnson, J.T. Lewandowski, Inorg. Chem. **24**, 3727–3729 (1985). https://doi.org/10.1021/ic00217a006
15. C.C. Stoumpos, D.H. Cao, D.J. Clark, J. Young, J.M. Rondinelli, J.I. Jang, J.T. Hupp, M.G. Kanatzidis, Chem. Mater. **28**, 2852–2867 (2016). https://doi.org/10.1021/acs.chemmater.6b00847
16. K.R. Kendall, C. Navas, J.K. Thomas, H.-C. zurLoye, Chem. Mater. **8**, 642–649 (1996). https://doi.org/10.1021/cm9503083
17. A. Forde, T. Inerbaev, E.K. Hobbie, D.S. Kilin, J. Am. Chem. Soc. **141**, 4388–4397 (2019). https://doi.org/10.1021/jacs.8b13385
18. J.P. Perdew, K. Burke, M. Ernzerhof, Phys. Rev. Lett. **78**, 1396–1396 (1997). https://doi.org/10.1103/PhysRevLett.78.1396
19. G. Kresse, D. Joubert, Phys. Rev. B **59**, 1758–1775 (1999). https://doi.org/10.1103/PhysRevB.59.1758
20. P.E. Blöchl, Phys. Rev. B **50**, 17953–17979 (1994). https://doi.org/10.1103/PhysRevB.50.17953
21. G. Kresse, J. Furthmüller, Comput. Mater. Sci. **6**, 15–50 (1996). https://doi.org/10.1016/0927-0256(96)00008-0
22. Y. Fu, W. Zheng, X. Wang, M.P. Hautzinger, D. Pan, L. Dang, J.C. Wright, A. Pan, S. Jin, J. Am. Chem. Soc. **140**, 15675–15683 (2018). https://doi.org/10.1021/jacs.8b07843
23. M. Kasha, Discuss. Faraday Soc. **9**, 14–19 (1950). https://doi.org/10.1039/DF9500900014